



# Long-lasting, fast-switchable photochromism in $\text{Na}_{0.5}\text{Bi}_{0.5}\text{TiO}_3$ induced by photocatalytic memory effect, and its subsequently enhanced piezoelectric response and catalytic performances

Lizhen Lu<sup>a</sup>, Haoyu Zhang<sup>a</sup>, Jinghui Wang<sup>b</sup>, Haolin Wang<sup>a</sup>, Qian Chen<sup>a</sup>, Jinbo Xue<sup>c</sup>, Qianqian Shen<sup>c</sup>, Chunliang Zhou<sup>d</sup>, Jian Ku Shang<sup>b</sup>, Qi Li<sup>a,\*</sup>

<sup>a</sup> Key Laboratory of Advanced Technologies of Materials (Ministry of Education), School of Materials Science and Engineering, Southwest Jiaotong University, Chengdu 610031, PR China

<sup>b</sup> Shenyang National Laboratory for Materials Science, Institute of Metal Research, Chinese Academy of Sciences, Shenyang 110016, PR China

<sup>c</sup> Key Laboratory of Interface Science and Engineering in Advanced Materials (Ministry of Education), College of Materials Science and Engineering, Taiyuan University of Technology, Taiyuan 030024, PR China

<sup>d</sup> Yantai Research Institute, Harbin Engineering University, Yantai 264000, PR China



## ARTICLE INFO

### Keywords:

$\text{Na}_{0.5}\text{Bi}_{0.5}\text{TiO}_3$   
Photochromism  
Photocatalytic memory effect  
Oxygen vacancies  
Photopiezocatalysis

## ABSTRACT

A ferroelectric ceramic material of  $\text{Na}_{0.5}\text{Bi}_{0.5}\text{TiO}_3$  was found to possess a pronounced, long-lasting, and fast-switchable photochromic behavior responsive to visible light. The working mechanism of its photochromism could be attributed to an interesting photocatalytic memory effect, during which photogenerated electrons were trapped by  $\text{Bi}^{3+}/\text{Ti}^{4+}$  and oxygen vacancies generated in  $\text{Na}_{0.5}\text{Bi}_{0.5}\text{TiO}_3$ . The release kinetics of trapped electrons could be modulated by controlling environment conditions to make its photochromism phenomenon both long-lasting and fast-switchable to meet various application requirements. In the meantime, the photochromism process changed its inner electronic structure, resulting in stronger oxidation capability, increased piezoelectric response, improved charge carrier separation and transfer, and more active oxygen species production. Thus, its photocatalytic, piezocatalytic and photopiezocatalytic performances were all significantly enhanced as demonstrated by its TC-HCl degradation performances. This work offered a novel approach to search for and design inorganic photochromic materials with good reversibility for various technical applications.

## 1. Introduction

Recently, an interesting photocatalytic memory effect has been found to exist in various photocatalytic material systems, which allows these photocatalysts to sustain activities for a certain duration time even after the light source is deactivated [1–5]. Its working mechanism relies on the storage of photogenerated electrons during irradiation and their gradual release in the absence of light. The controlled release of trapped electrons generates free radicals even after the light source is deactivated, which preserves the catalytic activity of the photocatalyst in dark for a long duration [6]. So, the internal electronic structure of the photocatalyst is changed by the photocatalytic memory effect for the duration time, while it could change back to its original status when the photocatalytic memory effect is off after the complete release of trapped electrons. Thus, long-lasting reversible property changes driven by light

illumination could happen in materials with the photocatalytic memory effect due to their reversible internal electronic structure changes, and their subsequently-generated novel functions could be expected to be utilized in various technologic areas, including photoelectricity, photomagnetism, photochromism, photomechanical actuation, and photopolymerization [3–14].

Photochromism has found a wide range of technical applications, such as optical information storage, optical switches, optical temperature sensors, and reusable erasable devices [15]. Various organic, inorganic, and organic-inorganic hybrid materials have been extensively investigated on their photochromic performances [16]. Among them, the research on inorganic photochromic materials has been increasing fast in recent years because they possess superior mechanical strength, thermal stability, and chemical stability compared with organic photochromic materials [17]. The fundamental physical process of their

\* Correspondence to: No. 111 Section 1, Northern Second Ring Road, Chengdu, Sichuan 610031, PR China.

E-mail address: [qiliu@swjtu.edu.cn](mailto:qiliu@swjtu.edu.cn) (Q. Li).

photochromic reactions involves the capture and release of photo-generated electrons and holes by color centers in them, which is reversible and could be achieved through alternating external stimuli [18]. Although photochromic phenomena had been found in some simple metal oxides such as  $V_2O_5$ ,  $WO_3$ ,  $TiO_2$ , and  $MoO_3$ , their poor charge separation and transfer efficiency resulted in limited reversibility, greatly restricting their applications [19–22]. Recently, the reversible photochromic properties of ferroelectric ceramic materials have received widespread attentions, and they were generally doped with rare earth elements to induce luminescence behavior [23]. These ferroelectric ceramics-based photochromic materials could not only exhibit rapid photochromic response time, but also possess excellent reversibility [24,25]. However, little research had been conducted on the photochromic behavior of pure-phase ferroelectric ceramics. Furthermore, these ferroelectric photochromic materials may also possess different catalytic capabilities, while their photochromic behaviors on their catalytic performances had not been investigated.

In this work,  $Na_{0.5}Bi_{0.5}TiO_3$  (NBT) ceramic powder was synthesized through a conventional solid-phase high-temperature calcination process. It was found that the  $ATiO_3$  perovskite type NBT ceramic powder exhibited a pronounced, long-lasting photochromic behavior responsive to visible light at room temperature. Its color-changing mechanism could be attributed to the photocatalytic memory effect, and the long-lasting property was beneficial for applications requiring a long-time color display. Its color change could also be switched back fast by a simple infrared light irradiation within seconds, beneficial for applications requiring a fast and easy erasing process. Furthermore, its photochromism also changed its inner electronic structure, which resulted in an enhanced piezoelectricity, better photogenerated charge carrier separation, and subsequent beneficial impacts on its catalytic properties. Consequently, it demonstrated enhanced tetracycline hydrochloride (TC-HCl) degradation performances by photocatalysis, piezocatalysis, and photopiezocatalysis after the photochromic process with good stability and reusability. Both experimental and theoretical analysis results suggested that oxygen vacancies generated during the photochromism process significantly enhanced the adsorption of  $O_2$  and  $H_2O$  on the NBT ceramic powder sample to increase the formation of active oxygen species of  $\cdot O_2$  and  $\cdot OH$  for the enhanced catalytic TC-HCl degradation performances.

## 2. Experimental section

### 2.1. Chemicals and materials

All the reagents were analytically pure and used without further purification. Sodium carbonate ( $Na_2CO_3$ , 99.5%), bismuth oxide ( $Bi_2O_3$ , 99.975%), titanium dioxide ( $TiO_2$ , 99.8%), and Tetracycline hydrochloride (TC-HCl, 99%) were purchased from Aladdin. Biochemical Co. (Shanghai, P. R. China). Dilute TC-HCl solutions were prepared with pure water.

### 2.2. Synthesis of $Na_{0.5}Bi_{0.5}TiO_3$ ceramic powder

$Na_{0.5}Bi_{0.5}TiO_3$  (NBT) ceramic powder was synthesized by a refined solid-phase calcination reaction method. First,  $Na_2CO_3$ ,  $Bi_2O_3$ , and  $TiO_2$  powders were weighed according to the stoichiometric ratio, and mixed in an agate tank by ball milling (250 r/min) with absolute ethanol and agate balls for 12 h. Next, the mixture was dried at 80 °C for 3 h and calcined at 900 °C for 4 h in a muffle furnace. Then, the obtained powders were ball-milled again for 12 h under same conditions. Subsequently, they were dried at 80 °C for 3 h, placed in an alumina crucible, and calcinated at 1130 °C under atmospheric conditions for 2 h. Finally, the obtained sample was ball-milled for 12 h for the last time under same conditions and dried at 80 °C for 3 h to obtain desired NBT ceramic powder.

### 2.3. Preparation of NBT ceramic sheets

To prepare NBT ceramic sheets, NBT ceramic powder was first granulated with 8 wt% polyvinyl alcohol (PVA) binder, and unidirectionally pressed into sheets of various sizes. Then, they were calcinated in a muffle furnace at 1130 °C for 2 h to obtain NBT ceramic sheets.

### 2.4. Material characterization

The sample's crystal structure was investigated by X-ray diffraction (XRD, Empyrean Alpha-1, Malvern Panalytic, Netherland) at a scanning speed of 0.02°. High-resolution transmission electron microscopy (HRTEM, JEM-2100 F, JEOL, Japan) was used to investigate the surface topographies, lattice fringes and selected-area electron diffraction (SAED) patterns. X-ray photoelectron spectroscopy (XPS) was conducted on a Thermo Scientific K-Alpha X-ray photoelectron spectrometer (Thermo Fisher, U.S.A.) with a monochromatized  $Al K\alpha$  X-ray source (1486.6 eV) to examine their surface chemical compositions and binding energies. The presence of oxygen vacancies was further detected by the electron paramagnetic resonance (EPR) spectrum (Bruker EMXplus-6/1, Germany) and the Raman spectrum (Horiba Lab RAM HREvolution, Japan) measurements. UV-vis reflectance spectra of samples were measured on a UV-vis spectrometer (UV-3600PLUS, Shimadzu Co., Ltd., Japan) with  $BaSO_4$  as the benchmark. Piezoresponse force microscopy (PFM) measurement was conducted with a Bruker Dimension Icon AFM (Germany). The electric field-induced polarization hysteresis ( $P-E$ ) loops were measured by a ferroelectric tester (Radian Technologies, Inc., Albuquerque, NM) to examine the piezoelectric properties of samples. The absorption intensity of the TC-HCl solution was characterized using a UV-vis spectrophotometer (UV-3600PLUS, Shimadzu Co., Ltd., Japan) and its concentration was determined by the comparison with the standard TC-HCl solution.

### 2.5. Photoelectrochemical measurements

Photoelectrochemical measurements were conducted on a CHI 760E electrochemical analyzer (Shanghai Chenhua Instrument Ltd., Shanghai, P. R. China) with 0.2 M  $Na_2SO_4$  solution as the electrolyte at room temperature. A conventional three-electrode configuration system was used, which included the working electrode (the NBT sample-loaded FTO glass), the counter electrode (Pt wire), and the reference electrode (the saturated  $Ag/AgCl$  electrode). The NBT sample-loaded FTO glass was prepared as follows: 20 mg sample was uniformly mixed with a solution of Nafion and ethanol (volume ratio of 1:10) by ultrasonication for 30 min, and then the mixture was coated on FTO glass. A 300 W Xenon lamp (PLS-SXE-300+, Beijing Perfect Light Technology Co., Ltd., Beijing, China) was used as the light source. Photocurrent transient response was measured on the open circuit voltage with the irradiation "on" and "off" for 20 s internal. Electrochemical impedance spectroscopy (EIS) measurement was conducted in the range of 0.01 Hz to 100 kHz. Mott-Schottky (M-S) analysis was carried out at two different frequencies (2000 Hz and 3000 Hz) to obtain the flat band potential values of the NBT sample before and after the photochromism process, respectively.

### 2.6. Catalytic TC-HCl decomposition experiments

The photocatalytic, piezocatalytic and photopiezocatalytic activities of the NBT ceramic powder before and after the photochromism process were assessed by its decomposition of a typical antibiotic (TC-HCl) under visible light illumination, ultrasonication, and visible light illumination with ultrasonication, respectively. In a typical experiment, 50 mg of the NBT powder sample was firstly added into 50 mL of the TC-HCl solution (10 mg/L), and the suspension was stirred in dark for 30 min to achieve the adsorption-desorption balance. Then, the suspension was treated by visible light illumination (under Xenon lamp

with light filter of 380 nm to 720 nm), ultrasonication (with an ultrasonic cleaner operated with 40 kHz and 180 W), and visible light illumination with ultrasonication, respectively. During the reaction process, 4 mL of the treated suspension was sampled at 10 min intervals and centrifuged for 5 min under 12000 rpm. Finally, 3 mL of the supernatant liquid was analyzed by the UV-3600PLUS UV-vis spectrophotometer.

### 2.7. Detection of active radicals in catalytic TC-HCl decomposition

To identify active species in the photocatalytic, piezocatalytic and piezophotocatalytic TC-HCl decomposition processes, benzoquinone (BQ, 0.5 mM), disodium ethylenediaminetetraacetate (EDTA, 1 mM), isopropanol (IPA, 1 mM) and sodium bromate ( $\text{NaBrO}_3$ , 1 mM) were used as scavengers for superoxide radicals ( $\cdot\text{O}_2^-$ ), holes ( $h^+$ ), hydroxyl radicals ( $\cdot\text{OH}$ ) and electrons ( $e^-$ ), respectively. Furthermore, the existences of  $\cdot\text{O}_2^-$ ,  $h^+$  and  $\cdot\text{OH}$  in the piezophotocatalytic TC-HCl decomposition process were also examined with the electron paramagnetic resonance (EPR) spectrum measurements (Bruker EMX plus, Germany).

### 2.8. DFT calculations

In this work, all density functional theory (DFT) calculations were conducted using the Vienna Ab Initio Simulation Package (VASP) code. The Perdew-Burke-Ernzerhof (PBE) functional, within the framework of the generalized gradient approximation (GGA), was employed to accurately describe the electronic exchange-correlation energy. The ionic cores were characterized using the projector augmented wave (PAW)

method. The calculated  $2 \times 2 \times 2$  supercell structures were subjected to periodic boundary conditions in the  $x$ - and  $y$ -directions. Additionally, in the  $z$ -direction, a separation of 15 Å vacuum height was introduced between the structure and its neighboring units. A basis set of plane waves was defined with an energy cutoff of 390 eV. For both structure optimization and energy calculations,  $K$ -points were specified at  $2 \times 2 \times 1$ . All computations were iterated until both the force and energy converged to values less than 0.03 eV Å<sup>-1</sup> and 10<sup>-5</sup> eV, respectively. The  $\text{O}_2$  and  $\text{H}_2\text{O}$  adsorption processes were further explored through DFT calculations to determine the adsorption energy ( $\Delta E_{\text{ads}}$ ) using the following Eq. (3) [26]:

$$\Delta E_{\text{ads}} = E_{\text{base-ads}} - (E_{\text{base}} + E_{\text{ads}}) \quad (1)$$

where  $E_{\text{base-ads}}$ ,  $E_{\text{base}}$ , and  $E_{\text{ads}}$  represent the total energy of the base-adsorption species, base, and adsorption species, respectively.

## 3. Results and discussion

### 3.1. Crystal structure and microstructure analysis of NBT ceramic powders

NBT ceramic powders were synthesized via a traditional solid calcination method. Fig. 1a shows the XRD pattern of NBT ceramic powders, which demonstrated that all diffraction peaks matched well with the standard diffraction peaks of pure monoclinic  $\text{Na}_{0.5}\text{Bi}_{0.5}\text{TiO}_3$  phase (PDF#46-0001) [27]. Thus, pure phase NBT ceramic powders with good crystallinity were synthesized through our approach. Fig. 1b

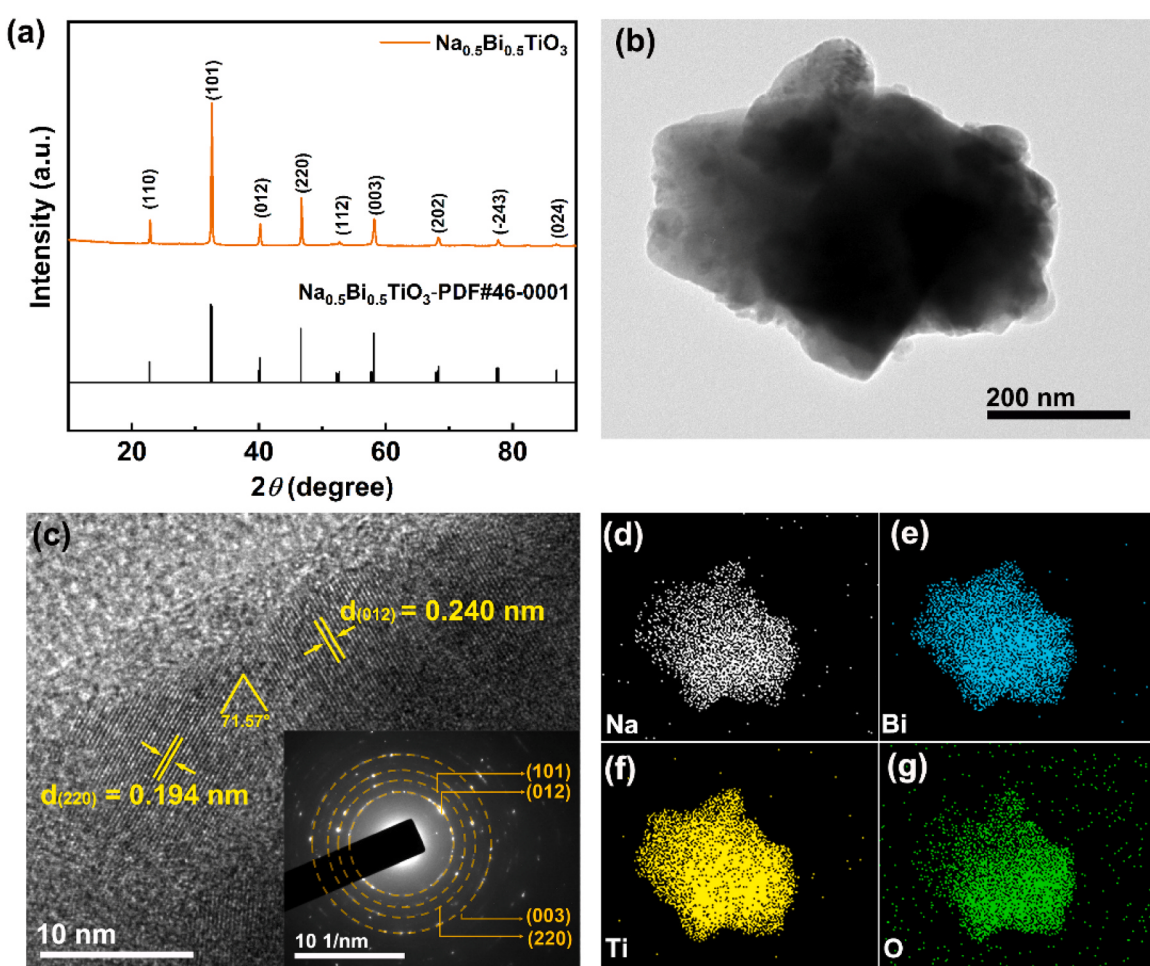


Fig. 1. (a) XRD pattern, (b) TEM image, (c) HRTEM image and (d) to (g) EDX elemental mapping images of the NBT ceramic powder sample. The inset image in (c) shows SAED pattern of the NBT ceramic powder sample.

shows the TEM image of NBT ceramic powder sample, which clearly demonstrated that it was composed of irregular aggregations of sub-micron size. Fig. 1c shows its high-resolution TEM (HRTEM) image, in which clear lattice fringes could be easily observed. The lattice spacing values of the two lattice fringes with the separation angle of  $71.57^\circ$  were determined at  $\sim 0.240$  nm and  $\sim 0.194$  nm, which matched well with (012) and (220) crystal facets of the pure monoclinic NBT phase, respectively. The inset image in Fig. 1c shows the selected area electron diffraction (SAED) pattern of the NBT ceramic powder sample. Continuous rings could be identified in it, which could be indexed with (101), (012), (003), and (220) crystal facets, respectively. Thus, TEM analysis clearly demonstrated the well-crystallized polycrystalline nature of NBT ceramic powders. Figs. 1d to 1g show the corresponding energy dispersive X-ray (EDX) elemental mapping images of the NBT ceramic powder sample, which confirmed the uniform distributions of Na, Bi, Ti, and O elements in it.

### 3.2. Long-lasting, switchable photochromic phenomenon of NBT ceramic powders

An interesting photochromic phenomenon was found on these pure NBT ceramic powders. When NBT ceramic powders were exposed to sunlight or visible light illumination, their color clearly changed from the original pale-yellow to brown quickly, and the color change could last for several days at room temperature before it finally changed back to the original color. Thus, it could maintain the color change under a normal storage environment for a long time, beneficial for applications requiring a long-time display. It was further found that a heat treatment at  $\sim 200$  °C for just 1 s or an infrared light illumination for just 5 s could largely accelerate the color switching back process, which demonstrated that the environment temperature had a crucial effect on the switchable photochromic behavior of NBT ceramic powders. Thus, the photochromic color change of NBT ceramic powders could be easily erased by a simple infrared light irradiation in a short time through raising the temperature, beneficial for applications requiring a fast and easy erasing process. Figure S1 in the supplementary material shows the reflective

intensity differences of an NBT ceramic sheet at 458 nm after being illuminated by visible light (405 nm) and infrared light alternatively for 10 times. It demonstrated that the NBT ceramic sheet had an excellent switchable photochromic behavior stability.

Because of its excellent switchable photochromic behavior, it could serve as a time-sensitive rewritable paper as shown in Fig. 2. Through illuminations by visible light (405 nm) and infrared light, cartoon characters, letters, and numbers could be designed and written onto NBT ceramic sheets in a straightforward photomask process. As shown in Fig. 2a, a panda character became distinctly visible on an NBT ceramic sheet following its exposure to the visible light illumination through a photomask of panda pattern. Fig. 2b shows the writing and erasing processes on NBT ceramic sheets. With the increase of visible light exposure time, both the panda character and letters of "SWJTU" became more and more vivid. After a 5 s exposure to infrared light, patterns written onto NBT ceramic sheets vanished, clearly demonstrating the rewritable nature of NBT ceramic sheets. Fig. 2c shows the capability to change the written patterns on NBT ceramic sheets by exposures to different light irradiations. For example, the digital number "8" was first written on the NBT ceramic sheet by the exposure to a 405 nm light irradiation through a photomask of "8". Then, an infrared light illumination for 5 s through a photomask of "-" successfully erased the central "-" in the digital number "8" and changed it to "0". By the same process, digital numbers of "2" and "3" were also successfully created by erasing parts of "8" through the use of infrared light illumination. These interesting examples clearly demonstrated the excellent switchable photochromic behavior of NBT ceramic powders for reversibility.

### 3.3. Long-lasting, switchable photochromic mechanism of NBT ceramic powders

The long-lasting, switchable photochromic mechanism of NBT ceramic powders was investigated. Figure S2 in the supplementary material shows the XRD pattern of the NBT ceramic powder sample with visible light (405 nm) exposure for 10 min, compared with that of the sample without prior irradiation. The comparison clearly illustrated that

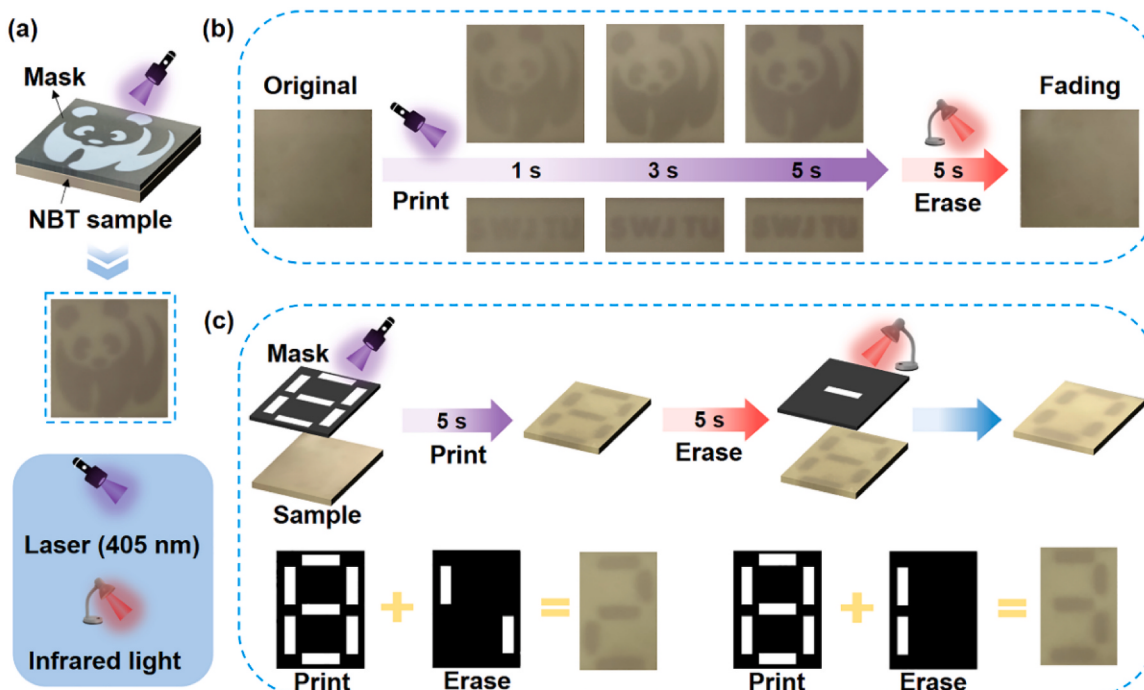


**Fig. 2.** (a) Schematic illustration of the photoprinting process on NBT ceramic sheets with a photomask. (b) The writing and erasing processes on NBT ceramic sheets by irradiations of visible light (405 nm) and infrared light, respectively. (c) The processes to change the written patterns on NBT ceramic sheets by exposures to different light irradiations.

both XRD patterns matched well with that of the pure monoclinic  $\text{Na}_0.5\text{Bi}_{0.5}\text{TiO}_3$  phase (PDF#46-0001), and there was no discernible difference between them. Thus, the photochromic color change observed in the NBT ceramic powder sample could not be attributed to its crystal structure change by visible light illumination.

X-ray photoelectron spectroscopy (XPS) analysis was carried out to investigate potential changes of the chemical states of NBT ceramic powders after being exposed to visible light for 10 min. Figure S3 in the [supplementary material](#) shows XPS survey spectra of the NBT ceramic powder sample without and with prior visible light irradiation. Both XPS spectra clearly revealed presences of signals belonging to Na, Bi, Ti, O, and C elements, and the C element signal originated from the surrounding environment. Figs. 3a to 3d present high-resolution XPS scans over Na 1 s, Bi 4 f, Ti 2p and O 1 s peaks of the NBT ceramic powder sample without and with prior visible light irradiation, respectively. It was evident that both Bi 4 f (see Fig. 3b) and Ti 2p peaks (see Fig. 3c) shifted towards the lower binding energy direction after the NBT ceramic powder sample was irradiated by visible light. As a visible-light-activated photocatalyst, electron and hole pairs could be generated in NBT under visible light illumination [28]. Thus, this observation implied that photogenerated electrons must migrate towards Bi and Ti elements in NBT under visible light irradiation and could be effectively trapped on them for an extended time duration, which indicated the occurrence of an interesting photocatalytic memory effect [29].

Figure S4a in the [supplementary material](#) shows the TC-HCl (5 mg/L) degradation curve by the NBT ceramic powder sample in dark after being exposed to visible light for 10 min initially. It demonstrated that the NBT ceramic powder sample after the photochromism process showed a clear TC-HCl degradation effect in dark, while the NBT

ceramic powder sample without the photochromism process showed no TC-HCl degradation effect in dark. This observation verified the existence of the photocatalytic memory effect in the NBT ceramic powder sample [6]. Figure S4b shows the electron spin resonance (EPR) measurement spectra of the NBT ceramic powder samples in dark before and after the photochromism process with 2,2,6,6-Tetramethylpiperidine N-oxide (TEMPO) as the capture agent for  $e^-$  (in water), respectively. It was found that the TEMPO characteristic peak intensity decreased in dark after the photochromism process, compared with that before the photochromism process. This comparison result indicated that electrons were released in dark by the NBT ceramic powder sample after the photochromism process, which further verified the existence of the photocatalytic memory effect in the NBT ceramic powder sample [2,6].

Consequently, the trapping of photogenerated electrons through the photocatalytic memory effect could result in the formation of oxygen vacancies (O<sub>v</sub>) in NBT ceramic powders due to the charge balance requirement in this material system [30]. Fig. 3d compares O 1 s XPS spectra of the NBT ceramic powder sample without and with prior visible light irradiation. Both of them could be best fitted into the combination of two peaks representing lattice oxygen and O<sub>v</sub>, respectively. The percentage of O<sub>v</sub> of the NBT ceramic powder sample had an obvious increase from ~ 42.0% initially to ~ 49.5% after being irradiated by visible light. Furthermore, its lattice oxygen peak also shifted to the lower binding energy direction by 0.4 eV after being irradiated by visible light, which indicated lattice oxygen bond fracture happened and oxygen vacancies were generated [30].

Electron paramagnetic resonance (EPR) spectroscopy and Raman spectroscopy were used to further confirm the O<sub>v</sub> creation in the NBT ceramic powder sample by visible light irradiation. Fig. 3e compares

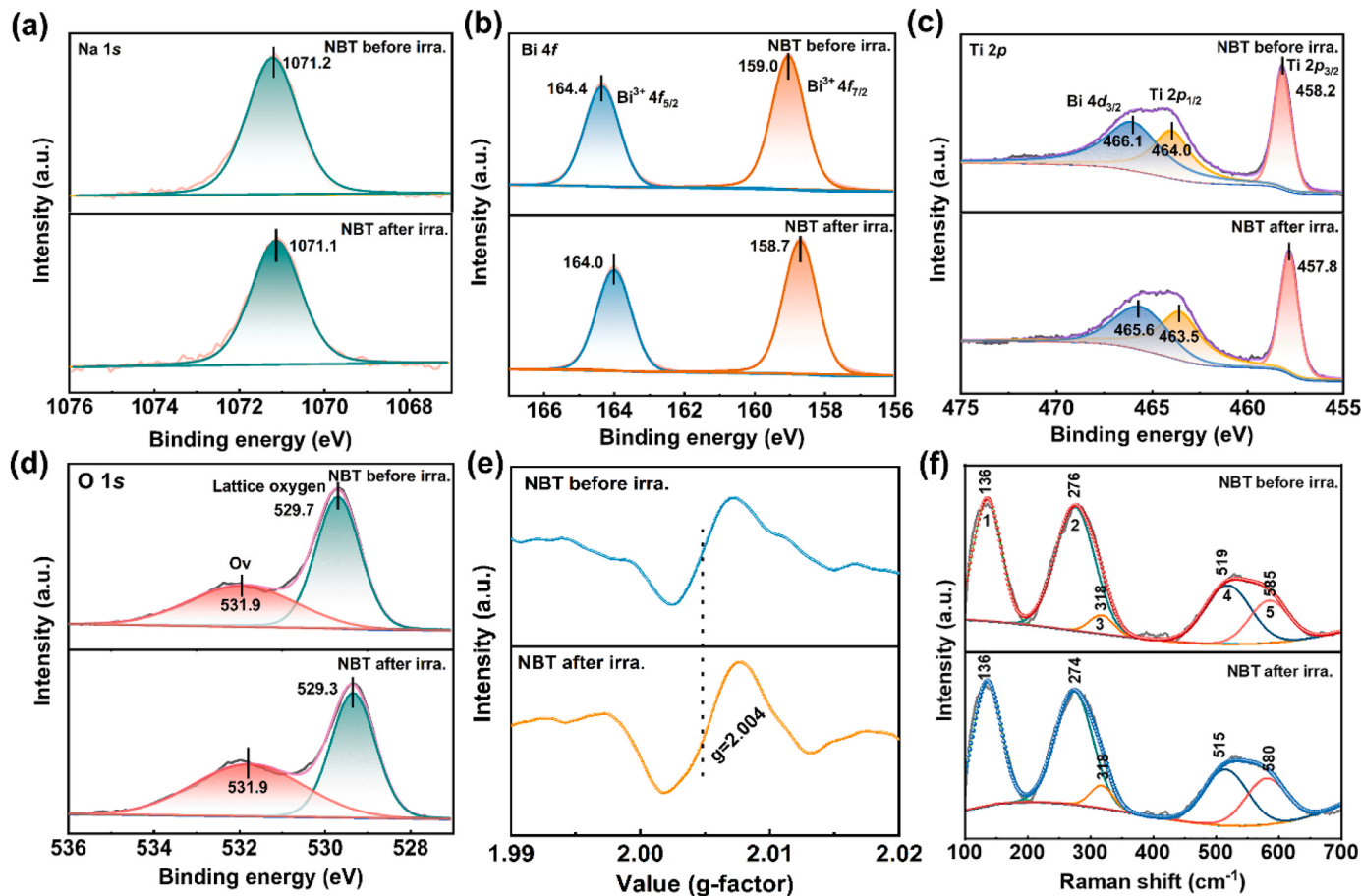


Fig. 3. (a) to (d) High-resolution XPS scans over Na 1 s (a), Bi 4 f (b), Ti 2p (c), and O 1 s (d) peaks, (e) EPR spectra and (f) Raman spectra of the NBT ceramic powder sample without and with prior visible light irradiation for 10 min, respectively.

EPR spectra of the NBT ceramic powder sample without and with prior visible light irradiation for 10 min. It demonstrated that the O<sub>V</sub> signal peak ( $g = 2.005$ ) intensity increased after the visible light irradiation, indicating that more O<sub>V</sub> were generated in the NBT ceramic powder sample by visible light irradiation. Fig. 3 f shows the Raman spectra of the NBT ceramic powder sample without and with prior visible light irradiation for 10 min. Although they were generally similar, differences could also be found between them. Especially, Raman bands dominated by vibrations involving mainly oxygen displacements moved towards lower wave numbers (from  $\sim 519 \text{ cm}^{-1}$  and  $\sim 585 \text{ cm}^{-1}$  to  $\sim 515 \text{ cm}^{-1}$  and  $\sim 580 \text{ cm}^{-1}$ , respectively) after being irradiated by visible light. It is well known that defects typically result in a reduction of the lattice vibration frequency, corresponding to a lower wave number shift in the Raman spectrum [31–33]. Thus, Raman spectrum analysis results also indicated the formation of oxygen defects in the NBT ceramic powder sample by visible light irradiation.

From above analysis results, the visible light irradiation did not change the crystal structure of the NBT ceramic powder sample, while it caused changes of chemical states and generation of oxygen vacancies in the sample through the photocatalytic memory effect. Due to the slow reaction kinetics of re-oxidizing Bi<sup>(3-δ)+</sup> to Bi<sup>3+</sup> and Ti<sup>(4-δ)+</sup> to Ti<sup>4+</sup> by oxygen at room temperature, the process for photogenerated O<sub>V</sub> to disappear was quite slow. Thus, O<sub>V</sub> generated by the photocatalytic memory effect in the NBT ceramic powder sample had a quite long life, which suggested that the photochromism in the NBT ceramic powder sample was long-lasting at room temperature. When the environment temperature increased ( $\sim 200 \text{ }^{\circ}\text{C}$  for just 1 s or under an infrared light illumination for just 5 s), the reaction kinetics of re-oxidizing Bi<sup>(3-δ)+</sup> to Bi<sup>3+</sup> and Ti<sup>(4-δ)+</sup> to Ti<sup>4+</sup> by oxygen largely increased, which resulted in the acceleration of the disappearance of photo-generated oxygen vacancies. Thus, the NBT ceramic powder sample could also show a fast

switchable photochromism.

### 3.4. Optical property and electronic structure changes in NBT ceramic powders after the photochromism process

UV-vis diffuse reflectance spectra of the NBT ceramic powder sample before and after the photochromism process were measured to explore their optical property differences. Fig. 4a shows that its reflectance curves before and after the photochromism process (exposure to visible light for 10 min) were quite close in the UV region till  $\sim 400 \text{ nm}$  and then remarkably decreased in the visible light range after the photochromism process, which was in accordance with its color change from the original pale-yellow to brown. Fig. 4b shows the band gap value determinations of the NBT ceramic powder sample before and after the photochromism process, respectively. Its Tauc Plots were constructed from its light absorbance data, and its band gap values were determined by Tauc's formula as given by Eq. (2):

$$\alpha h\nu = A (h\nu - E_g)^{n/2} \quad (2)$$

where  $\alpha$ ,  $h\nu$ ,  $A$ , and  $E_g$  are light absorption coefficient, photon energy, proportionality constant, and band gap energy, respectively [34]. Figure S5 in the supplementary material shows the energy band structure of the NBT sample obtained by DFT calculations. It demonstrated that the conduction band minimum (CBM) of NBT was located between G-M, while the valence band maximum (VBM) was located between K-G. Thus, CBM and VBM of the NBT sample were located at different high symmetry points, which clearly demonstrated that the NBT sample was an indirect band gap semiconductor [35]. This calculation result was in accordance with the literature and  $n$  equals 4 for the indirect semiconductor of NBT [36]. It was found that the photochromism process did not change its band gap value, which was determined at  $\sim 3.18 \text{ eV}$  no

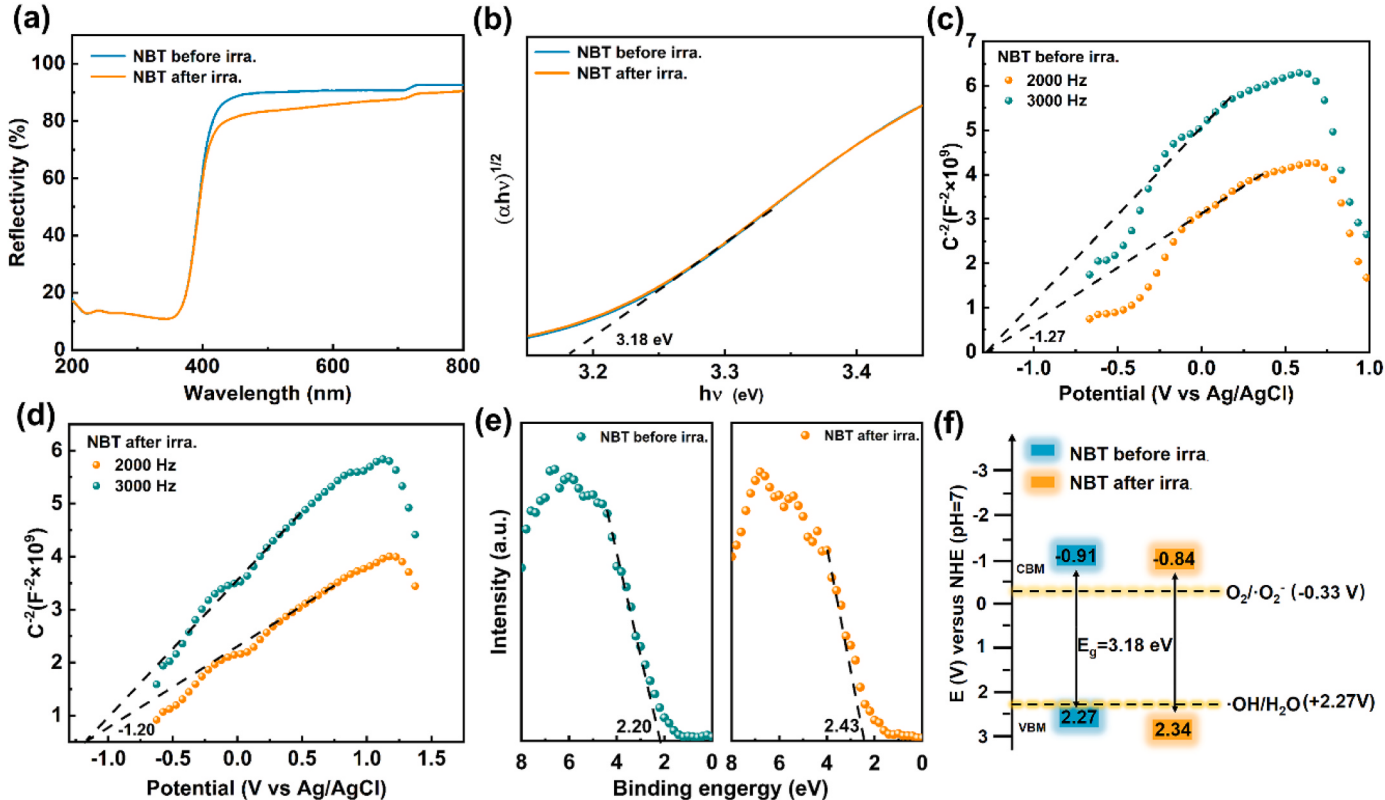


**Fig. 4.** (a) Reflectance spectra and (b) Tauc Plots constructed from the light absorbance data of the NBT ceramic powder sample before and after the photochromism process, respectively. (c) and (d) Mott-Schottky plots of the NBT ceramic powder sample (c) before and (d) after the photochromism process vs. the Ag/AgCl reference electrode measured at 2000 Hz and 3000 Hz, respectively. (e) XPS valence band spectra and (f) Energy band structures of the NBT ceramic powder sample before and after the photochromism process, respectively.

matter the photochromism process happened or not.

Figs. 4c and 4d show Mott-Schottky plots of the NBT ceramic powder sample before and after the photochromism process *vs.* the Ag/AgCl reference electrode at 2000 Hz and 3000 Hz, respectively. The positive slopes of these Mott-Schottky curves indicated that the NBT ceramic powder sample was an *n*-type semiconductor no matter the photochromism process happened or not [37]. Its flat band potentials ( $E_{fb}$ ) *vs.* the Ag/AgCl electrode ( $E_{Ag/AgCl}$ ) could be determined from the intercepts of these Mott-Schottky curves at  $\sim -1.27$  V before the photochromism process and  $\sim -1.20$  V after the photochromism process, respectively. Its flat band potentials *vs.* the normal hydrogen electrode ( $E_{fb}$  (*vs.* NHE)) could be determined according to Eq. (3) [38,39]:

$$E_{fb} (\text{vs. NHE}) = E_{fb} + E_{Ag/AgCl}^0 + 0.0591 \times \text{pH} \quad (3)$$

where  $E_{Ag/AgCl}^0$  was 0.197 eV and the solution pH was determined at 6.1. Thus, the  $E_{fb}$  (*vs.* NHE) values of the NBT ceramic powders sample before and after the photochromism process were calculated at  $\sim -0.71$  V and  $\sim -0.64$  V, respectively.

For the *n*-type semiconductor, its conduction band ( $E_{CB}$ ) value is generally more negative than its  $E_{fb}$  value for  $\sim 0.2$  eV [40]. Combined with the band gap values determined by Tauc plots, the conduction band minimum (CBM) and valence band maximum (VBM) values of the NBT ceramic powder sample before the photochromism process could be estimated at  $\sim -0.91$  V and  $\sim 2.27$  V, respectively, while that after the photochromism process could be estimated at  $\sim -0.84$  V and  $\sim 2.34$  V, respectively. Fig. 4e shows XPS valence band spectra of the NBT ceramic powder sample, which demonstrated that its VBM values were  $\sim 2.20$  V and  $\sim 2.43$  V before and after the photochromism process, respectively. Thus, its VBM values measured from XPS valence band spectra were very close (within 0.1 eV) to that calculated by its band gap values and CBM

values determined from its M-S plots, which indicated the data accuracy. Fig. 4f shows the energy band structure diagrams of the NBT ceramic powder sample before and after the photochromism process, respectively, which indicated that it had a stronger oxidation capability after the photochromism process due to the more positive VBM.

### 3.5. Piezoelectric response enhancement in NBT ceramic powders after the photochromism process

Because  $\text{Bi}^{3+}$  and  $\text{Ti}^{4+}$  trapped photogenerated electrons and oxygen vacancies were generated subsequently, changes of inner electronic structure occurred in the NBT ceramic powder sample after the photochromism process induced by the photocatalytic memory effect. Thus, the photochromism process could affect the piezoelectric response of the NBT ceramic powder sample. Figs. 5a and 5b show the piezoelectric response force microscopy (PFM) measurement results of the PFM phase and amplitude hysteresis loops of the NBT ceramic powder sample before and after the photochromism process, respectively. The NBT ceramic powder sample had well-defined piezoresponse phase reversal hysteresis loops and the characteristic amplitude-voltage butterfly loops for both conditions [41,42], which demonstrated that its piezoelectric nature was not affected by the photochromism process induced by visible light irradiation. However, its piezoelectric response became notably enhanced by the photochromism process. The NBT ceramic powder sample initially exhibited a domain phase switching of  $\sim 210^\circ$  under a ramped voltage loop ranging from  $-60$  V to  $60$  V (see the blue line in Fig. 5a), while its domain phase switching reached  $\sim 210^\circ$  under a much smaller ramped voltage loop ranging from  $-30$  V to  $30$  V after the photochromism process (see the blue line in Fig. 5b). Thus, the changes of inner electronic structure in the NBT ceramic powder sample

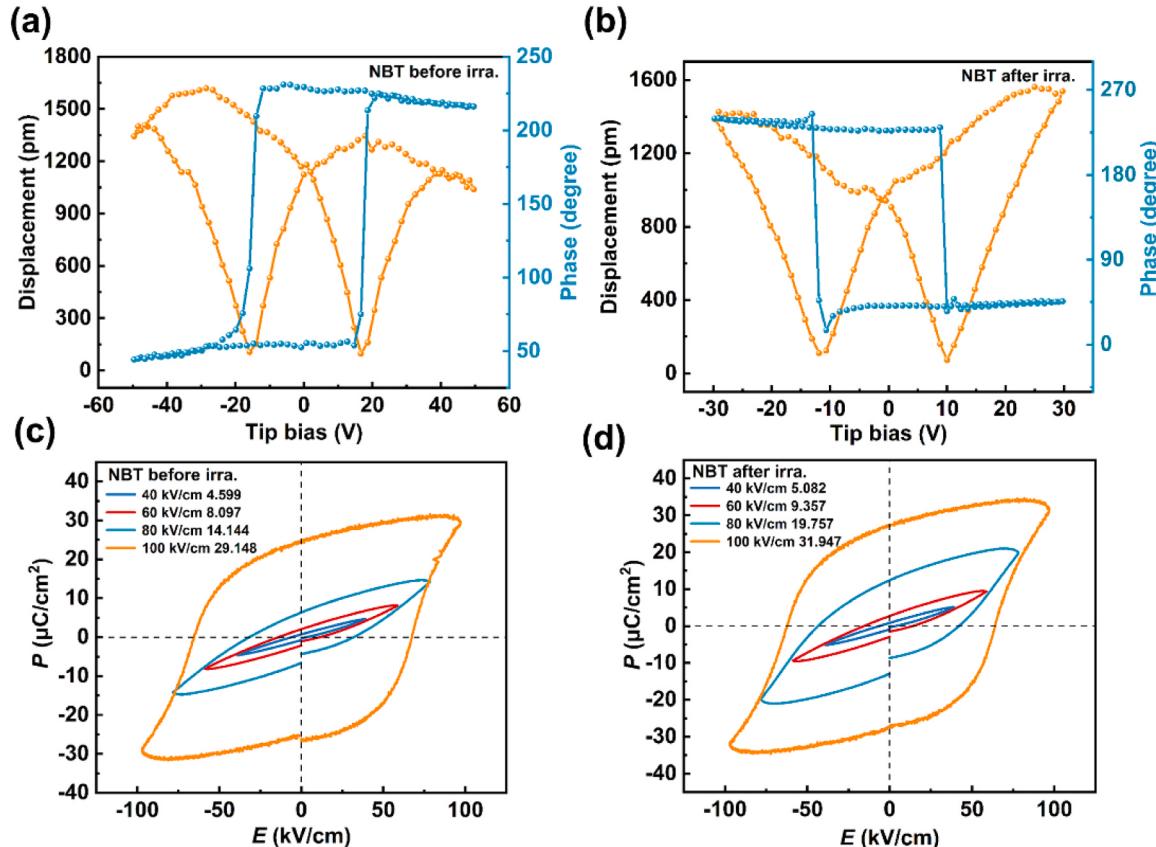


Fig. 5. PFM phase hysteresis loops and amplitude hysteresis loops of the NBT ceramic powder sample (a) before and (b) after the photochromism process, respectively. P-E loops of the NBT ceramic sheet sample measured at room temperature under different electric fields (c) before and (d) after the photochromism process, respectively.

led to a reduction in its coercive field, thereby rendering it more prone to polarization. From the slope of the displacement-voltage curve, the maximum effective piezoelectric coefficient ( $d_{33}$ ) could be obtained to quantitatively present a sample's piezoelectricity [43]. It was found that the  $d_{33}$  value of the NBT ceramic powder sample increased to  $\sim 83.7$  pm/V after the photochromism process from its original value of  $\sim 59.2$  pm/V, representing an increase to  $\sim 141\%$ . Thus, its  $d_{33}$  value increase clearly demonstrated that its piezoelectricity enhanced after the photochromism process.

The polarization-electric field ( $P$ - $E$ ) curves of the NBT ceramic sheet sample were measured at 50 Hz and room temperature under a series of electric fields both before and after the photochromism process as shown in Figs. 5c and 5d, respectively, which demonstrated that it had the typical  $P$ - $E$  loops of a piezoelectric material [44]. With the increase of the electric field, its remnant polarization ( $P_r$ ) and maximum polarization ( $P_{max}$ ) values increased no matter the photochromism process happened or not. Thus, its  $P$ - $E$  curve measurement result also demonstrated that its piezoelectric nature was not affected by the photochromism process induced by visible light irradiation. Furthermore, at the same electric field strength, its  $P_r$  and  $P_{max}$  values were always larger after the photochromism process under the same applied electric field strength, which indicated that it would exhibit a stronger polarization response under external force after the photochromism process. Thus, these results demonstrated that the photochromism process induced by the photocatalytic memory effect could result in an enhanced internal polarization in the NBT ceramic powder sample, thereby promoting the separation of charge carriers in piezocatalysis and photopiezocatalysis.

### 3.6. Photogenerated charge carrier separation and transfer enhancement in NBT ceramic powders after the photochromism process

Photogenerated charge carrier separation and transfer behavior in the NBT ceramic powder sample was investigated with photoelectrochemical characterization methods. Fig. 6a shows the photocurrent densities of the NBT ceramic powder sample before and after the photochromism process, respectively, which demonstrated that its photocurrent density was notably higher after the photochromism process. This result confirmed that the separation efficiency of photogenerated charge carriers in the NBT ceramic powder sample was improved by the photochromism process due to the creation of additional  $O_2$  and the enhanced internal polarization. Fig. 6b shows its Nyquist plots before and after the photochromism process either in dark or under visible light illumination, respectively. No matter in dark or

under visible light irradiation, the arc radius of its Nyquist plots after the photochromism process was smaller than that of the sample before the photochromism process. The inset image of Fig. 6b shows the equivalent circuit of the impedance diagram, and the fitting parameters of these Nyquist plots by ZView software [45] had been summarized in Table S1 in the supplementary material.  $R_{ct}$  values of the NBT sample before the photochromism process were  $22.63\ \Omega$  in dark and  $17.01\ \Omega$  under visible light illumination, respectively, while that after the photochromism process were reduced to  $22.48\ \Omega$  in dark and  $12.40\ \Omega$  under visible light illumination, respectively. These observations demonstrated that the photochromism process resulted in the reduction of interface resistance and the improvement in charge transport efficiency in the NBT ceramic sample.

### 3.7. Enhanced catalytic activities of NBT ceramic powders after the photochromism process

Due to its light activation capability and piezoelectric nature, the NBT ceramic powder sample could be applied for photocatalysis, piezocatalysis, and their synergistic photopiezocatalysis as demonstrated by its catalytic degradations of TC-HCl before and after the photochromism process, respectively. Figure S6 in the supplementary material shows the light absorption curves of TC-HCl solutions under different catalytic treatments for a series of treatment times, and the corresponding analysis results were summarized in Fig. 7. Fig. 7a shows the photocatalytic TC-HCl degradation performance of the NBT ceramic powder sample under visible light illumination before and after the photochromism process, respectively, compared with that only under visible light illumination without the sample presence. After 50 min under only visible light illumination without the sample presence, a slight degradation of TC-HCl was observed with a high residual percentage of  $\sim 92\%$ . When the NBT ceramic powder sample was present, its adsorption of TC-HCl in dark was minimum, while it effectively degraded TC-HCl by the photocatalysis both before and after the photochromism process. After 50 min treatment, the residual percentage of TC-HCl was  $\sim 33\%$  and  $\sim 23\%$  for the NBT ceramic powder sample before and after the photochromism process, respectively. Its photocatalytic activity enhancement by the photochromism process could be further demonstrated quantitatively by comparing its initial TC-HCl photocatalytic degradation rates before and after the photochromism process at the beginning of the degradation with the same initial TC-HCl concentration, which were determined at  $\sim 0.294\ mg/(g\cdot min)$  and  $\sim 0.498\ mg/(g\cdot min)$ , respectively.

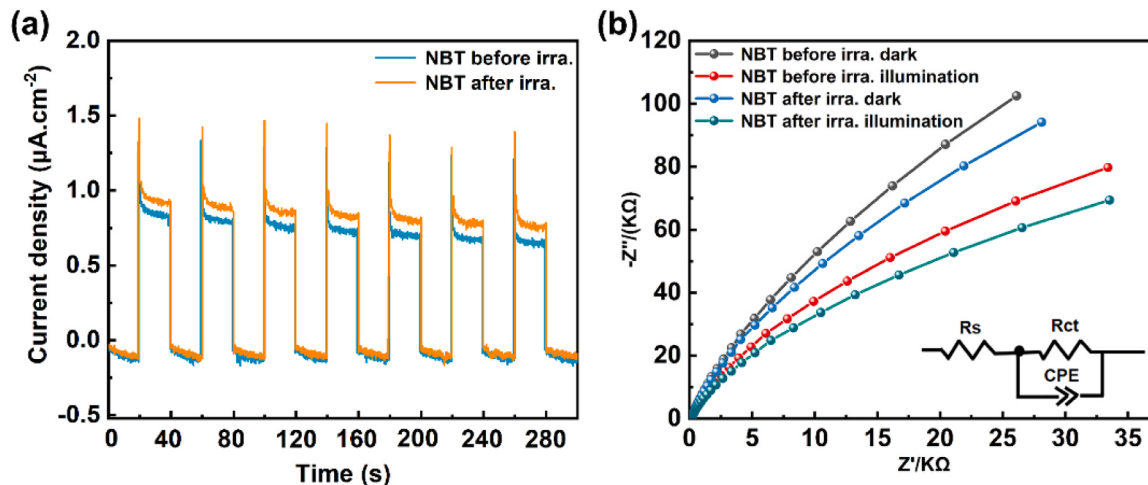
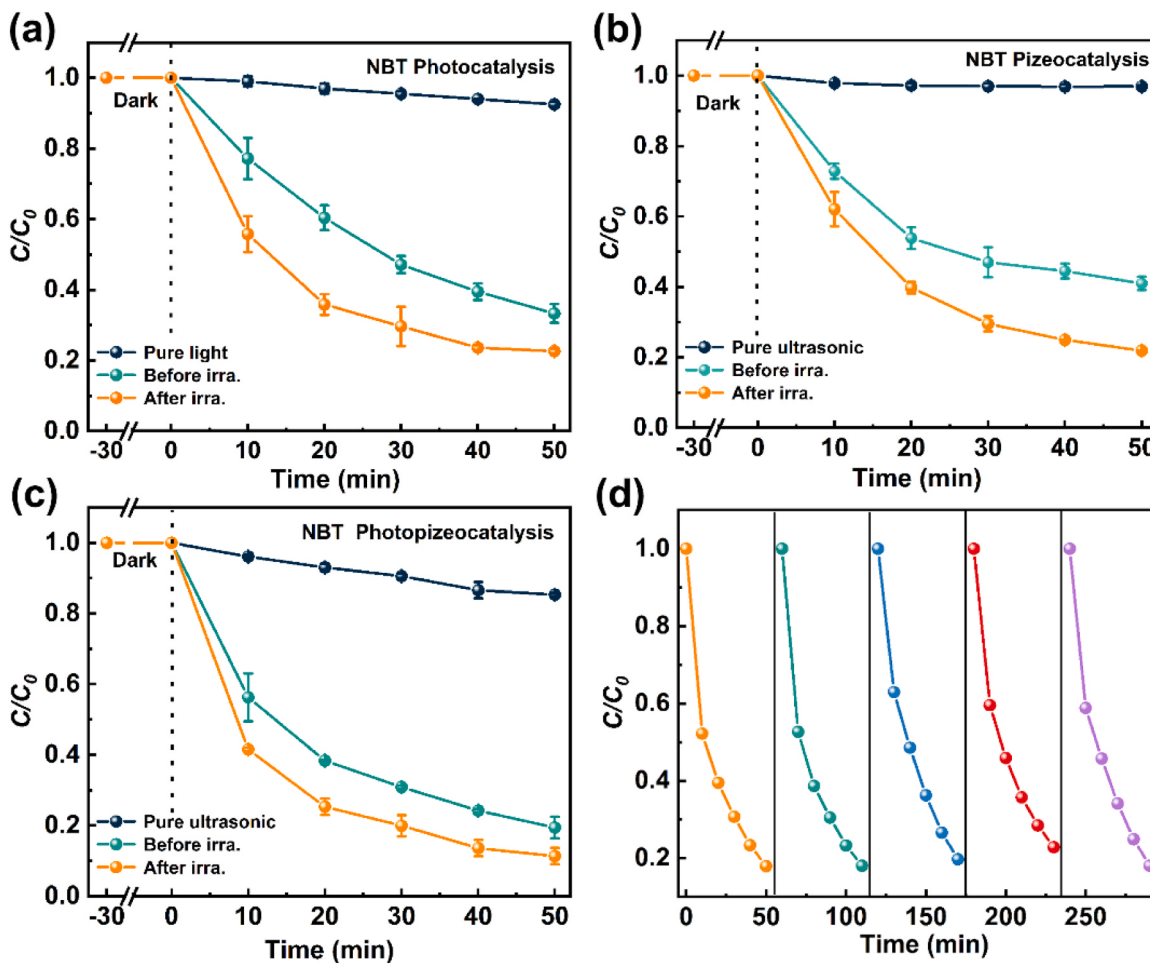


Fig. 6. (a) Photocurrent densities of the NBT ceramic powder sample before and after the photochromism process. (b) Nyquist plots of the NBT ceramic powder sample before and after the photochromism process either in dark or under visible light illumination, respectively (The inset image shows the equivalent circuit of the impedance diagram).



**Fig. 7.** (a) to (c) The residual percentages of TC-HCl (initial concentration of 10 mg/L) during the photocatalytic, piezocatalytic, and photopiezocatalytic degradations by the NBT ceramic sample before and after the photochromism process, respectively. (d) Photopiezocatalytic TC-HCl degradation performance stability of the NBT ceramic sample after the photochromism process in five consecutive runs.

Fig. 7b shows the piezocatalytic TC-HCl degradation performance of the NBT ceramic powder sample under ultrasonication before and after the photochromism process, respectively, compared with that under ultrasonication without the sample presence. It demonstrated that ultrasonication could only cause a slight degradation of TC-HCl (the residual percentage of  $\sim 97\%$  after 50 min treatment), while the NBT ceramic powder sample effectively degraded TC-HCl by the piezocatalysis. After 50 min treatment, the residual percentage of TC-HCl was  $\sim 41\%$  and  $\sim 22\%$  for the NBT ceramic powder sample before and after the photochromism process, respectively. Its piezocatalytic activity enhancement by the photochromism process could be further demonstrated quantitatively by comparing its initial TC-HCl piezocatalytic degradation rates before and after the photochromism process at the beginning of the degradation with the same initial TC-HCl concentration, which were determined at  $\sim 0.337 \text{ mg}/(\text{g}\cdot\text{min})$  and  $\sim 0.443 \text{ mg}/(\text{g}\cdot\text{min})$ , respectively.

Fig. 7c shows the synergistic photopiezocatalytic TC-HCl degradation performance of the NBT ceramic powder sample under both visible light illumination and ultrasonication before and after the photochromism process, respectively, compared with that under both visible light illumination and ultrasonication without the sample presence. It demonstrated that visible light illumination and ultrasonication together could cause a moderate degradation of TC-HCl (the residual percentage of  $\sim 85\%$  after 50 min treatment), while the NBT ceramic powder sample effectively degraded TC-HCl by the synergistic photopiezocatalysis. After 50 min treatment, the residual percentage of TC-HCl was  $\sim 19\%$  and  $\sim$

11% for the NBT ceramic powder sample before and after the photochromism process, respectively. Its photopiezocatalytic activity enhancement by the photochromism process could be further demonstrated quantitatively by comparing its initial TC-HCl photopiezocatalytic degradation rates before and after the photochromism process at the beginning of the degradation with the same initial TC-HCl concentration, which were determined at  $\sim 0.489 \text{ mg}/(\text{g}\cdot\text{min})$  and  $\sim 0.618 \text{ mg}/(\text{g}\cdot\text{min})$ , respectively. Thus, the photochromism process did enhance the photocatalytic, piezocatalytic, and photopiezocatalytic TC-HCl degradation performances of the NBT ceramic powder sample, and the synergistic photopiezocatalytic degradation had the best performance.

The synergistic photopiezocatalytic TC-HCl degradation percentage of the NBT ceramic powder sample shown above was not higher than the combination of its photocatalytic degradation percentage and piezocatalytic degradation percentage (see Figs. 7a to 7c), which was found to be due to the relatively low initial TC-HCl concentration used. Figure S7 shows residual percentages of TC-HCl solutions during the photocatalytic, piezocatalytic, and photopiezocatalytic degradations by the NBT ceramic sample after the photochromism process, respectively, with a two-time higher initial TC-HCl concentration of 20 mg/L. Under a higher initial TC-HCl concentration, the initial photocatalytic, piezocatalytic, and photopiezocatalytic degradation rates of TC-HCl by the NBT ceramic sample after the photochromism process could be determined at  $\sim 0.325 \text{ mg}/(\text{g}\cdot\text{min})$ ,  $\sim 0.158 \text{ mg}/(\text{g}\cdot\text{min})$  and  $\sim 0.557 \text{ mg}/(\text{g}\cdot\text{min})$ , respectively. Table S2 in the supplementary material summarizes the

degradation percentages of TC-HCl (initial concentration of 20 mg/L) by the NBT ceramic powder sample after the photochromism process under photocatalysis, piezocatalysis, and photopiezocatalysis, respectively. These degradation effect analysis results demonstrated clearly that the photopiezocatalytic TC-HCl degradation effect was higher than the combination of the photocatalytic TC-HCl degradation and the piezocatalytic TC-HCl degradation. Thus, the “1+1>2” synergistic effect in the TC-HCl degradation between the piezocatalysis and the photocatalysis could be observed on the NBT ceramic powder sample when the pollutant concentration was relatively high.

Fig. 7d shows the photopiezocatalytic TC-HCl degradation performances of the NBT ceramic powder sample after the photochromism process for 5 consecutive runs, which clearly demonstrated that it had relatively stable performances. Figure S8a compares XRD patterns of the NBT ceramic powder sample before and after 5 consecutive photopiezocatalytic TC-HCl degradation experiments, which demonstrated that they were generally identical. Figure S8b to S8f show the XPS survey spectrum and high-resolution XPS scans over Na 1 s, Bi 4 f, Ti 2p

and O 1 s peaks of the NBT ceramic powder sample after the photochromism process when the 5 consecutive photopiezocatalytic TC-HCl degradation experiments finished, which were also very similar to that of its fresh state as shown in Figure S3 and Fig. 3. Especially, it could be found from Figure S8e that the percentage of O<sub>v</sub> of the NBT ceramic powder sample was ~ 52%, which was even higher than its fresh of ~ 49.5%. Thus, oxygen vacancies created by the visible light illumination of 10 min through the photocatalytic memory effect could be kept and even increased during the photopiezocatalytic TC-HCl degradation process due to the continuous visible light irradiation in this process. Thus, the performance enhancement of the NBT ceramic powder sample by the photochromism process was stable, beneficial for its repeated uses in potential applications.

### 3.8. Active species detection and catalytic TC-HCl degradation mechanism

The degradation of TC-HCl during these catalytic processes could be

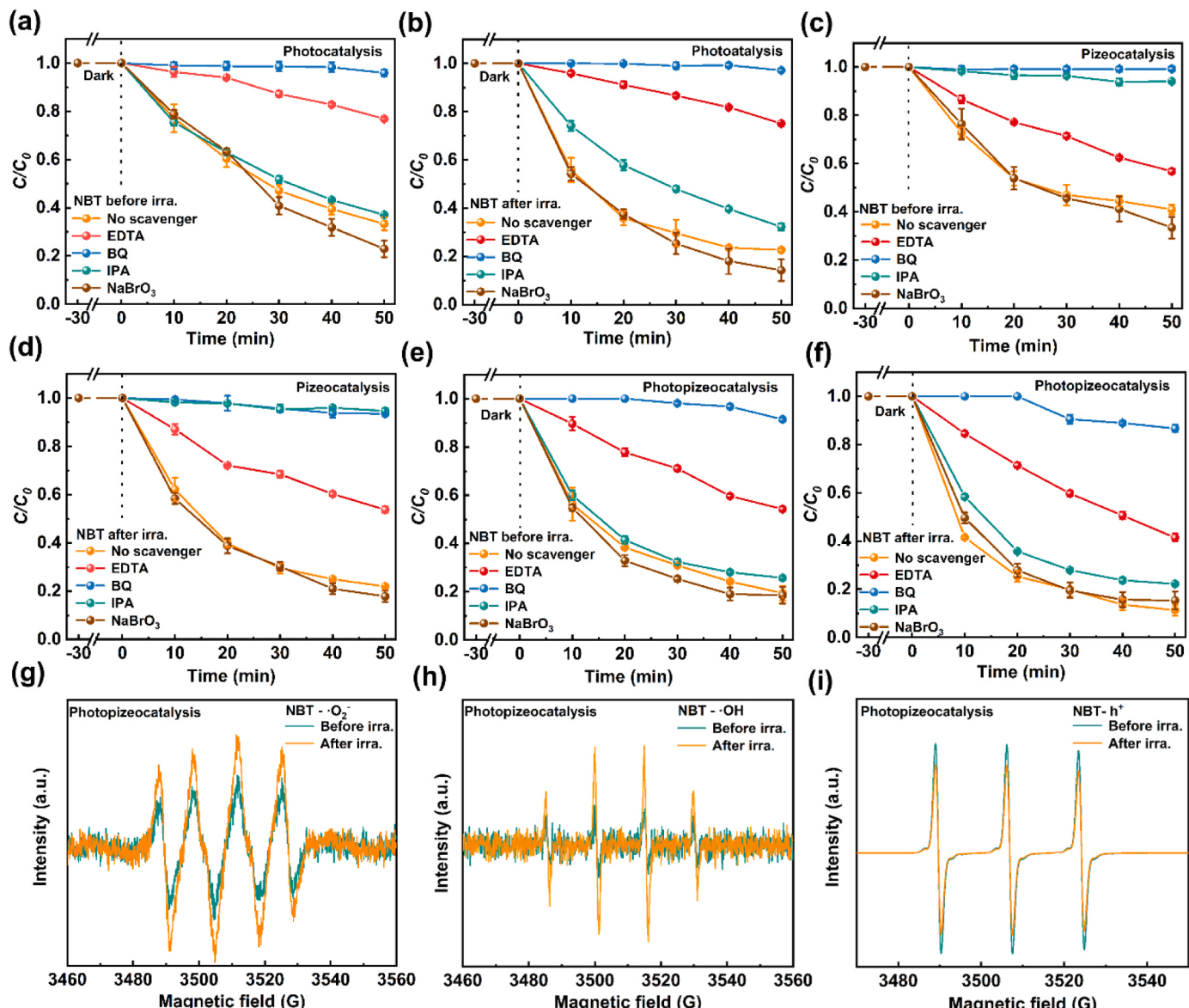


Fig. 8. The residual percentages of TC-HCl under (a) and (b) photocatalytic, (c) and (d) piezocatalytic, and (e) and (f) photopiezocatalytic treatments by the NBT ceramic powder sample before and after the photochromism process, respectively, without and with four kinds of active species scavengers. EPR spectra of (g) DMPO-·O<sub>2</sub><sup>-</sup>, (h) DMPO-OH and (i) TEMPO-h<sup>+</sup> signals in the photopiezocatalysis process of the NBT ceramic powder sample before and after the photochromism process, respectively.

attributed to the creation of reactive oxygen species [46]. Therefore, their generation in these catalytic processes was explored to investigate the role of free radicals in various catalytic processes to understand their mechanisms. Figs. 8a and 8b show the residual percentages of TC-HCl under the photocatalytic treatment by the NBT ceramic powder sample before and after the photochromism process without and with four kinds of active species scavengers of BQ (to capture  $\cdot\text{O}_2$ ), NaBrO<sub>3</sub> (to capture  $e^-$ ), IPA (to capture  $\cdot\text{OH}$ ), and EDTA (to capture  $h^+$ ), respectively. It was found that the presence of NaBrO<sub>3</sub> had no obvious hindering effect on the photocatalytic degradation of TC-HCl, while both BQ and EDTA could largely hinder the photocatalytic degradation of TC-HCl by the NBT ceramic powder sample no matter the photochromism process happened or not. Thus, both  $\cdot\text{O}_2$  and  $h^+$  played major roles in the photocatalytic degradation of TC-HCl by the NBT ceramic powder sample before and after the photochromism process, while  $e^-$  did not directly participate in the photocatalytic degradation of TC-HCl. Interestingly, IPA showed a clear hindering effect on the photocatalytic degradation of TC-HCl by the NBT ceramic powder sample after the photochromism process, while it showed no obvious hindering effect when no photochromism process happened in the NBT ceramic powder sample. This observation suggested that the photochromism process was beneficial to the generation of  $\cdot\text{OH}$  by the NBT ceramic powder sample, which was in accordance with its effect to result in a more positive VBM to over the  $\cdot\text{OH}$  generation potential requirement as shown in Fig. 4f.

Figs. 8c and 8d show the residual percentages of TC-HCl under the piezocatalytic treatment by the NBT ceramic powder sample before and after the photochromism process without and with four kinds of active species scavengers, respectively. It was also found that the presence of NaBrO<sub>3</sub> had no obvious hindering effect on the piezocatalytic degradation of TC-HCl by the NBT ceramic powder sample no matter the photochromism process happened or not, which suggested that  $e^-$  did not directly participate in the piezocatalytic degradation of TC-HCl. BQ, IPA and EDTA could all hinder the piezocatalytic degradation of TC-HCl by the NBT ceramic powder sample no matter the photochromism process happened or not, while BQ and IPA showed stronger hindering effect than EDTA. This observation suggested that  $\cdot\text{O}_2$  and  $\cdot\text{OH}$  played major roles in the piezocatalytic degradation of TC-HCl by the NBT ceramic powder sample, while the effect of  $h^+$  was weaker. Thus, the piezocatalysis of the NBT ceramic powder sample preferred to generate  $\cdot\text{OH}$ , which came from the oxidation of H<sub>2</sub>O by  $h^+$ .

Figs. 8e and 8f show the residual percentages of TC-HCl under the synergistic photopiezocatalytic treatment by the NBT ceramic powder sample before and after the photochromism process without and with four kinds of active species scavengers, respectively. As expected, BQ showed the best hindering effect and EDTA showed the medium hindering effect no matter the photochromism process happened or not, while IPA only still showed a clear hindering effect when the photochromism process happened. This observation also suggested that photocatalysis dominated the photopiezocatalytic TC-HCl degradation process because main active species in it were the same as that in the photocatalysis process, while the piezocatalysis by ultrasonication helped to generate more radicals and facilitate the charge carrier separation and transfer.

Electron spin resonance (EPR) measurements were further conducted to further verify the existence of these active species in the photopiezocatalysis process by the NBT ceramic powder samples before and after the photochromism process. 5,5-Dimethyl-1-pyrroline N-oxide (DMPO) was used as the capture agent for  $\cdot\text{O}_2$  (in methanol) and  $\cdot\text{OH}$  (in water), and 2,2,6,6-Tetramethylpiperidine N-oxide (TEMPO) was used as the capture agent for  $h^+$  (in water). Figs. 8g and 8h shows that signal intensities of DMPO- $\cdot\text{O}_2$  and DMPO- $\cdot\text{OH}$  got obviously enhanced after the photochromism process happened in the NBT ceramic powder sample, indicating more  $\cdot\text{O}_2$  and  $\cdot\text{OH}$  were generated in its photopiezocatalysis process. For the TEMPO signal, however,  $h^+$  would react with TEMPO to reduce the peak intensity. Thus, a decrease of the TEMPO characteristic peak intensity indicates the generation of  $h^+$ .

Fig. 8i shows that the TEMPO characteristic peak intensity decreased after the photochromism process happened in the NBT ceramic powder sample, indicating more  $h^+$  were generated in its photopiezocatalysis process. These observation results were as expected, and consistent with the enhanced TC-HCl degradation performance of the NBT ceramic powder sample after the photochromism process and the results of active species scavenger experiments.

### 3.9. DFT calculations

The photochromism process in the NBT ceramic powder sample by the photocatalytic memory effect was beneficial for the generation of more O<sub>v</sub> in the NBT ceramic powder sample. To further investigate the impact of O<sub>v</sub> on its catalytic activities, DFT calculations were used to explore the charge difference distribution and absorption energy of O<sub>2</sub> and H<sub>2</sub>O molecules on surfaces of the NBT ceramic powder samples with different O<sub>v</sub> concentrations by selectively removing one (NBT-O<sub>v1</sub>) or two (NBT-O<sub>v2</sub>) oxygen atoms from the ideal NBT structure (NBT), respectively. Figs. 9a and 9b show the charge difference distributions of O<sub>2</sub> and H<sub>2</sub>O on ideal NBT, NBT-O<sub>v1</sub>, and NBT-O<sub>v2</sub> samples, where the blue and yellow regions indicated electron accumulation and depletion, respectively. It could be found that the interactions between NBT and O<sub>2</sub>/H<sub>2</sub>O got stronger when O<sub>v</sub> were introduced into NBT, and the NBT-O<sub>v2</sub> sample with most O<sub>v</sub> exhibited the strongest interaction, beneficial for the subsequent generation of reactive oxygen species. Figs. 9c and 9d summarize the calculated adsorption energy values of O<sub>2</sub> and H<sub>2</sub>O on the surface of the NBT ceramic powder samples with different O<sub>v</sub> concentrations, respectively. With the increase of O<sub>v</sub> concentration, the adsorption energy values of O<sub>2</sub> on NBT increased from -0.99 eV to -1.98 eV, and the adsorption energy values of H<sub>2</sub>O on NBT increased from -1.24 eV to -2.38 eV. The  $E_{\text{ads}}$  increase of negative values indicated that O<sub>v</sub> could significantly enhance the thermodynamic favorability for the adsorption of O<sub>2</sub> and H<sub>2</sub>O on NBT [47], which could effectively enhance the adsorption of O<sub>2</sub> and H<sub>2</sub>O and subsequently increase the formation of active oxygen species of  $\cdot\text{O}_2$  and  $\cdot\text{OH}$ . The DFT calculations results were consistent with experimental findings, which further illustrated the working mechanism of the photochromism process on the catalytic performance enhancement of the NBT ceramic powder samples.

## 4. Conclusion

In summary, a pronounced photochromic behavior responsive to visible light at room temperature was found in the pure phase ferroelectric Na<sub>0.5</sub>Bi<sub>0.5</sub>TiO<sub>3</sub> (NBT) ceramic powder. Its color-changing mechanism could be attributed to an interesting photocatalytic memory effect, which resulted in its long-lasting color change property at room temperature due to the slow release of trapped photogenerated electrons. Its color change could also be switched back within seconds by a simple infrared light irradiation through the acceleration of the release of trapped photogenerated electrons. Furthermore, its inner electronic structure was changed by its long-lasting photochromism, which was found to result in more positive VBM, stronger piezoelectric response, and improved separation and transfer of charge carriers. Oxygen vacancies were generated with the photochromism process, which enhanced the adsorption of O<sub>2</sub> and H<sub>2</sub>O molecules on the NBT ceramic powder surface and subsequently increased the production of active oxygen species of  $\cdot\text{O}_2$  and  $\cdot\text{OH}$ . Thus, the catalytic performance of the NBT ceramic powder was significantly enhanced by the photochromism process as demonstrated in its better catalytic degradations of TC-HCl through the photocatalysis, piezocatalysis, and photopiezocatalysis processes, respectively. This work demonstrated a novel strategy to search for and design inorganic photochromic ceramic materials with long-lasting and fast-switchable properties through the photocatalytic memory effect, and proposed a novel approach to enhance their catalytic properties by the photochromism process through the modulation

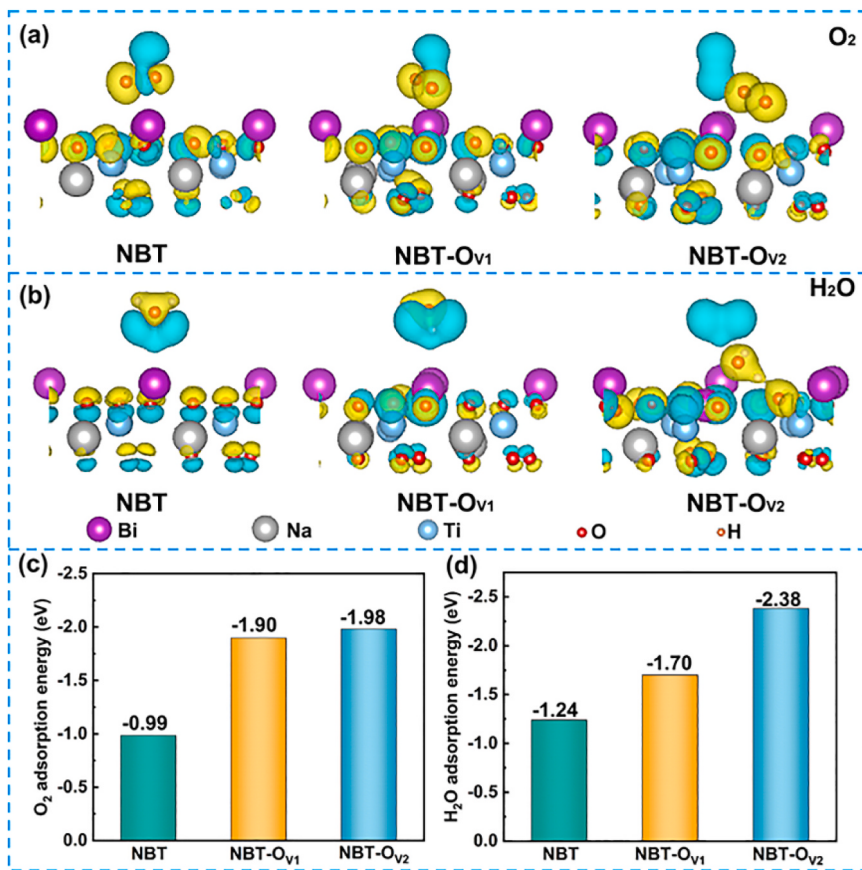


**Fig. 9.** Density functional theory calculations results: Charge difference distributions of (a)  $O_2$  and (b)  $H_2O$  molecules adsorbed on surfaces of NBT, NBT-O<sub>v1</sub> and NBT-O<sub>v2</sub> samples, respectively. The adsorption energies of (c)  $O_2$  and (d)  $H_2O$  molecules on surfaces of NBT, NBT-O<sub>v1</sub> and NBT-O<sub>v2</sub> samples, respectively.

of their inner electronic structures.

#### CRediT authorship contribution statement

**Haolin Wang:** Formal analysis. **Qian Chen:** Data curation. **Jinbo Xue:** Software, Methodology. **Qianqian Shen:** Software, Methodology. **Chunliang Zhou:** Validation. **Jian Ku Shang:** Writing – review & editing, Methodology. **Qi Li:** Writing – review & editing, Supervision, Funding acquisition, Conceptualization. **Lizhen Lu:** Writing – original draft, Investigation. **Haoyu Zhang:** Data curation. **Jinghui Wang:** Data curation.

#### Declaration of Competing Interest

The authors declare that they have no known competing financial interests or personal relationships that could have appeared to influence the work reported in this paper.

#### Data Availability

Data will be made available on request.

#### Acknowledgements

This study was supported by the National Natural Science Foundation of China (Grant No. 52272125), the Fundamental Research Funds for the Central Universities (Grant No. YX1199912371401-009), and Sichuan Science and Technology Program (Grant No. 2020YJ0259). We would like to thank Analysis and Testing Center of Southwest Jiaotong University for the assistance on material characterization.

#### Appendix A. Supporting information

Supplementary data associated with this article can be found in the online version at [doi:10.1016/j.apcatb.2024.124240](https://doi.org/10.1016/j.apcatb.2024.124240).

#### References

- [1] Q. Li, Y.W. Li, Z.Q. Liu, R.C. Xie, J.K. Shang, Memory antibacterial effect from photoelectron transfer between nanoparticles and visible light photocatalyst, *J. Mater. Chem. B* 20 (2010) 1068–1072, <https://doi.org/10.1039/b917239d>.
- [2] F. Feng, W.Y. Yang, S. Gao, C.X. Sun, Q. Li, Postillumination activity in a single-phase photocatalyst of Mo-doped  $TiO_2$  Nanotube array from its photocatalytic “memory”, *ACS Sustain. Chem. Eng.* 6 (2018) 6166–6174, <https://doi.org/10.1021/acssuschemeng.7b04845>.
- [3] W.Y. Yang, Y. Chen, S. Gao, L.C. Sang, R.G. Tao, C.X. Sun, J.K. Shang, Q. Li, Postillumination activity of  $Bi_2WO_6$  in the dark from the photocatalytic “memory” effect, *J. Adv. Ceram.* 10 (2021) 355–367, <https://doi.org/10.1007/s40145-020-0448-8>.
- [4] H.Q. Ma, W.Y. Yang, S. Gao, Z.F. Lin, Z.Y. Mo, C. Li, J.K. Shang, Q. Li, Photoirradiation-induced capacitance enhancement in the  $h\text{-}WO_3\text{/}Bi_2WO_6$  submicron rod heterostructure under simulated solar illumination and its postillumination capacitance enhancement retention from a photocatalytic memory effect, *ACS Appl. Mater. Interfaces* 13 (2021) 57214–57229, <https://doi.org/10.1021/acsami.1c17386>.
- [5] A.A. Khan, M. Tahir, N. Khan, LDH-based nanomaterials for photocatalytic applications: a comprehensive review on the role of bi/trivalent cations, anions, morphology, defect engineering, memory effect, and heterojunction formation, *J. Energy Chem.* 84 (2023) 242–276, <https://doi.org/10.1016/j.jecchem.2023.04.049>.
- [6] Q. Li, Y.W. Li, P.G. Wu, R.C. Xie, J.K. Shang, Palladium oxide nanoparticles on nitrogen-doped titanium oxide: accelerated photocatalytic disinfection and post-illumination catalytic “memory”, *Adv. Mater.* 20 (2008) 3717–3723, <https://doi.org/10.1002/adma.200800685>.
- [7] Q. Shen, X.F. Huang, J.B. Liu, C.Y. Guo, G.H. Zhao, Biomimetic photoelectrocatalytic conversion of greenhouse gas carbon dioxide: two-electron reduction for efficient formate production, *Appl. Catal. B Environ.* 201 (2017) 70–76, <https://doi.org/10.1016/j.apcatb.2016.08.008>.

[8] K. Nakamura, T. Oshikiri, K. Ueno, Y.M. Wang, Y. Kamata, Y. Kotake, H. Misawa, Properties of plasmon-induced photoelectric conversion on a  $\text{TiO}_2/\text{NiO}$  p-n junction with au nanoparticles, *J. Phys. Chem. Lett.* 7 (2016) 1004–1009, <https://doi.org/10.1021/acs.jpclett.6b00291>.

[9] S. Ohkoshi, H. Tokoro, Photomagnetism in cyano-bridged bimetal assemblies, *Acc. Chem. Res.* 45 (2012) 1749–1758, <https://doi.org/10.1021/ar300068k>.

[10] G.S. Patrin, N.V. Volkov, G.A. Petrakovskii, Photomagnetic effects in doped hematite crystals, *J. Magn. Magn. Mater.* 140-144 (1995) 2143–2144, [https://doi.org/10.1016/0304-8853\(94\)01160-5](https://doi.org/10.1016/0304-8853(94)01160-5).

[11] L. Wang, Q. Li, Photochromism into nanosystems: towards lighting up the future nanoworld, *Chem. Soc. Rev.* 47 (2018) 1044–1097, <https://doi.org/10.1039/C7CS00630F>.

[12] A. Viernstein, M. Kubicek, M. Morgenbesser, G. Walch, G.C. Brunauer, J. Fleig, High-temperature photochromism of Fe-doped  $\text{SrTiO}_3$  caused by UV-induced bulk stoichiometry changes, *Adv. Funct. Mater.* 29 (2019) 1900196, <https://doi.org/10.1002/adfm.201900196>.

[13] F. Zhang, L.Y. Zhu, Z.A. Li, S.Y. Wang, J.P. Shi, W.L. Tang, N. Li, J.Q. Yang, The recent development of vat photopolymerization: a review, *Addit. Manuf.* 48 (2021) 102423, <https://doi.org/10.1016/j.addma.2021.102423>.

[14] F. Fan, W.Y. Yang, S. Gao, L.G. Zhu, Q. Li, Photoinduced reversible lattice expansion in W-doped  $\text{TiO}_2$  through the change of its electronic structure, *Appl. Phys. Lett.* 112 (2018) 061904, <https://doi.org/10.1063/1.5019774>.

[15] P. Li, Z. Zhang, X.Y. Gao, H.Q. Sun, D.F. Peng, H. Zou, Q.W. Zhang, X.H. Hao, Fast self-bleaching  $\text{Nb}_2\text{O}_5$ -based photochromics for high security dynamic anti-counterfeiting and optical storage applications, *Chem. Eng. J.* 435 (2022) 134801, <https://doi.org/10.1016/j.cej.2022.134801>.

[16] R. Pardo, M. Zayat, D. Levy, Photochromic organic-inorganic hybrid materials<sup>†</sup>, *Chem. Soc. Rev.* 40 (2011) 672–687, <https://doi.org/10.1039/C0CS00065E>.

[17] W. Tang, C.D. Zuo, C.Y. Ma, Y.Z. Wang, Y.K. Li, X.Y. Yuan, E.G. Wang, Z.C. Wen, Y. G. Cao, Designing photochromic materials with high photochromic contrast and large luminescence modulation for hand-rewritable information displays and dual-mode optical storage, *Chem. Eng. J.* 435 (2022) 134670, <https://doi.org/10.1016/j.cej.2022.134670>.

[18] Q.W. Zhang, H.Q. Sun, X.S. Wang, X.H. Hao, S.L. An, Reversible luminescence modulation upon photochromic reactions in rare-earth doped ferroelectric oxides by *in situ* photoluminescence spectroscopy, *ACS Appl. Mater. Interfaces* 7 (2015) 25289–25297, <https://doi.org/10.1021/acsami.5b07345>.

[19] J. Gomez-Hermoso-de-Mendoza, H.S. Barud, J. Gutierrez, A. Tercjak, Flexible photochromic cellulose triacetate based bionanocomposites modified with sol-gel synthesized  $\text{V}_2\text{O}_5$  nanoparticles, *Carbohydr. Polym.* 208 (2019) 50–58, <https://doi.org/10.1016/j.carbpol.2018.12.045>.

[20] S.F. Wang, W.R. Fan, Z.C. Liu, A.B. Yu, X.C. Jiang, Advances on tungsten oxide based photochromic materials: strategies to improve their photochromic properties, *J. Mater. Chem. C* 6 (2018) 191–212, <https://doi.org/10.1039/C7TC04189F>.

[21] Y. Ohko, T. Tatsuma, T. Fujii, K. Naoi, C. Niwa, Y. Kubota, A. Fujishima, Multicolour photochromism of  $\text{TiO}_2$  films loaded with silver nanoparticles, *Nat. Mater.* 2 (2003) 29–31, <https://doi.org/10.1038/nmat796>.

[22] L. Zheng, Y. Xu, D. Jin, Y. Xie, Novel metastable hexagonal  $\text{MoO}_3$  nanobelts: synthesis, photochromic, and electrochromic properties, *Chem. Mater.* 21 (2009) 5681–5690, <https://doi.org/10.1021/cm9023887>.

[23] Q.W. Zhang, X.W. Zheng, H.Q. Sun, W.Q. Li, X.S. Wang, X.H. Hao, S.L. An, Dual-mode luminescence modulation upon visible-light-driven photochromism with high contrast for inorganic luminescence ferroelectrics, *ACS Appl. Mater. Interfaces* 8 (2016) 4789–4794, <https://doi.org/10.1021/acsami.5b12262>.

[24] F.Y. Yu, Y. Chi, P. Wang, B.W. Ma, X. Wu, C. Lin, C.L. Zhao, M. Gao, T.F. Lin, Q. W. Zhang, Highly responsive photochromic behavior with large coloration contrast in Ba/Sn co-doped ( $\text{K}_{0.5}\text{Na}_{0.5}\text{NbO}_3$ ) transparent ceramics, *Ceram. Int.* 48 (2022) 18899–18908, <https://doi.org/10.1016/j.ceramint.2022.03.169>.

[25] Y. Zhu, H.Q. Sun, Q.N. Jia, L.L. Guan, D.F. Peng, Q.W. Zhang, X.H. Hao, Site-selective occupancy of  $\text{Eu}^{2+}$  toward high luminescence switching contrast in  $\text{BaMgSiO}_4$ -based photochromic materials, *Adv. Opt. Mater.* 9 (2021) 2001626, <https://doi.org/10.1002/adom.202001626>.

[26] Q. Tang, J. Wu, X.Z. Chen, R. Sanchis-Gual, A. Veciana, C. Franco, D. Kim, I. Surin, J. Pérez-Ramírez, M. Mattera, A. Terzopoulou, N. Qin, M. Vukomanovic, B. J. Nelson, J. Puigmartí-Luis, S. Pané, Tuning oxygen vacancies in  $\text{Bi}_4\text{Ti}_3\text{O}_12$  nanosheets to boost piezo-photocatalytic activity, *Nano Energy* 108 (2023) 108202, <https://doi.org/10.1016/j.nanoen.2023.108202>.

[27] K. Liu, W.G. Ma, F.F. Liu, H. Tan, Z.M. Dou, C. Samart, S. Kongparakul, G.Z. Zhang, S.L. Jiang, P.Y. Fan, H.B. Zhang, Boosting electric-field-induced strain of dual templates-textured ( $\text{Na}_{1/2}\text{Bi}_{1/2}\text{TiO}_3$ )-based lead-free piezoceramics by polarization coupling, *J. Eur. Ceram. Soc.* 42 (2022) 6466–6477, <https://doi.org/10.1016/j.jeurceramsoc.2022.07.035>.

[28] Y. Jiang, S.J. Zhou, S.S. Mofarah, R.M. Niu, Y.L. Sun, A. Rawal, H.Y. Ma, K.L. Xue, X.Q. Fang, C.Y. Toe, W.F. Chen, Y.S. Chen, J.M. Cairney, R. Rahman, Z.B. Chen, P. Koshy, D.Y. Wang, C.C. Sorrell, Efficient and stable piezo-photocatalytic splitting of water and seawater by interfacial engineering of  $\text{Na}_{0.5}\text{Bi}_{0.5}\text{TiO}_3/\text{Na}_{0.5}\text{Bi}_{4.5}\text{Ti}_4\text{O}_{15}$  self-generated heterojunctions, *Nano Energy* 116 (2023) 108830, <https://doi.org/10.1016/j.nanoen.2023.108830>.

[29] L.Z. Lu, H.Y. Zhang, Z. Sun, J.H. Wang, H.L. Wang, J.B. Xue, Q.Q. Shen, Q. Li, Creation of robust oxygen vacancies in 2D ultrathin  $\text{BiOBr}$  nanosheets by irradiation through photocatalytic memory effect for enhanced  $\text{CO}_2$  reduction, *Chem. Eng. J.* 477 (2023) 146892, <https://doi.org/10.1016/j.cej.2023.146892>.

[30] X. Zhang, Y. Zhang, Z.Y. Feng, J.M. Zhao, Z.M. Yang, X. Wang, W.S. Wang, Self-accelerating photocharge separation in  $\text{BiOBr}$  ultrathin nanosheets for boosting photoreversible color switching, *Chem. Eng. J.* 428 (2022) 131235, <https://doi.org/10.1016/j.cej.2021.131235>.

[31] J.Y. Wu, H.B. Zhang, C.H. Huang, C.W. Tseng, N. Meng, V. Koval, Y.C. Chou, Z. Zhang, H.X. Yan, Ultrahigh field-induced strain in lead-free ceramics, *Nano Energy* 76 (2020) 105037, <https://doi.org/10.1016/j.nanoen.2020.105037>.

[32] L. Venkudu, N. Raja, D.E. Jain Ruth, A. Rashid, N.V. Giridharan, B. Sundarakannan,  $\text{Fe}^{3+}$ - and  $\text{Nb}^{5+}$ -substituted  $\text{Na}_{0.5}\text{Bi}_{0.5}\text{TiO}_3$ : a route toward enhanced ferroelectric photovoltaic response in  $\text{Al}/\text{NbFT}/\text{Ag}$  Solar Cell through reduced bandgap and controlled oxygen vacancy, *Energy Technol.* 11 (2023) 2300616, <https://doi.org/10.1002/ente.202300616>.

[33] S. Singh, A. Kaur, P. Kaur, L. Sing, Oxygen vacancies induced anomalies in the structural, ferroelectric and magnetic behaviour of sol-gel derived  $\text{LaCoO}_3$  modified  $\text{Na}_{0.5}\text{Bi}_{0.5}\text{TiO}_3$  ceramics, *Mater. Chem. Phys.* 279 (2022) 125754, <https://doi.org/10.1016/j.matchemphys.2022.125754>.

[34] J.F. Guayaquil-Sosa, Benito Serrano-Rosales, P.J. Valadés-Pelayo, H. de Lasa, Photocatalytic hydrogen production using mesoporous  $\text{TiO}_2$  doped with Pt, *Appl. Catal. B Environ.* 211 (2017) 337–348, <https://doi.org/10.1016/j.apcatb.2017.04.029>.

[35] Z.R. Miao, Q.L. Wang, Y.F. Zhang, L.P. Meng, X.X. Wang, In situ construction of S-scheme  $\text{AgBr}/\text{BiOBr}$  heterojunction with surface oxygen vacancy for boosting photocatalytic  $\text{CO}_2$  reduction with  $\text{H}_2\text{O}$ , *Appl. Catal. B Environ.* 301 (2022) 120802, <https://doi.org/10.1016/j.apcatb.2021.120802>.

[36] Y. Jiang, W.F. Chen, H.Y. Ma, H.J. Ren, S. Lim, X.X. Lu, G. Bahmanrokh, S. Mofarah, D.Y. Wang, P. Koshy, C.C. Sorrell, Effect of Bi/Ti ratio on  $(\text{Na}_{0.5}\text{Bi}_{0.5})\text{TiO}_3/\text{Bi}_4\text{Ti}_3\text{O}_{12}$  heterojunction formation and photocatalytic performance, *J. Environ. Chem. Eng.* 9 (2021) 106532, <https://doi.org/10.1016/j.je.2021.106532>.

[37] J. Suchanicz, K. Kluczenska-Chmielarz, D. Sitko, G. Jaglo, Electrical transport in lead-free  $\text{Na}_{0.5}\text{Bi}_{0.5}\text{TiO}_3$  ceramics, *J. Adv. Ceram.* 10 (2021) 152–165, <https://doi.org/10.1007/s40145-020-0430-5>.

[38] T. Giannakopoulou, I. Papailias, N. Todorova, N. Boukos, Y. Liu, J.G. Yu, C. Trapalis, Tailoring the energy band gap and edges' potentials of  $\text{g-C}_3\text{N}_4/\text{TiO}_2$  composite photocatalysts for NO<sub>x</sub> removal, *Chem. Eng. J.* 310 (2017) 571–580, <https://doi.org/10.1016/j.cej.2015.12.102>.

[39] D. Majhia, K. Dasa, A. Mishra, R. Dhiman, B.G. Mishra, One pot synthesis of  $\text{CdS}/\text{BiOBr}/\text{Bi}_2\text{O}_2\text{CO}_3$ : A novel ternary double Z-scheme heterostructure photocatalyst for efficient degradation of atrazine, *Appl. Catal. B Environ.* 260 (2020) 118222, <https://doi.org/10.1016/j.apcatb.2019.118222>.

[40] C.H. Wen, D.G. Li, J.P. Zhong, Z.Q. Wang, S.B. Huang, H.J. Liu, J.Q. Wu, P. Chen, W.Y. Lv, G.G. Liu, In situ synthesis of S-scheme  $\text{AgBr}/\text{BiOBr}$  for efficient degradation of sulfonamide antibiotics: synergistic effects of oxygen vacancies and heterojunctions promote exciton dissociation, *Chem. Eng. J.* 450 (2022) 138075, <https://doi.org/10.1016/j.cej.2022.138075>.

[41] Z. Zhu, Y.T. Xu, J.P. Li, G.Z. Cao, Ferroelectricity and piezoelectricity of  $\text{Na}_{0.5}\text{Bi}_{0.5}\text{TiO}_3$  nanotube arrays: implications for functional electronic devices, *ACS Appl. Nano Mater.* 4 (2021) 1294–1304, <https://doi.org/10.1021/acsnano.0c02878>.

[42] D.M. Liu, Y.W. Song, Z.J. Xin, G.X. Liu, C.C. Jin, F.K. Shan, High-piezocatalytic performance of eco-friendly  $(\text{Bi}_{1/2}\text{Na}_{1/2})\text{TiO}_3$ -based nanofibers by electrospinning, *Nano Energy* 65 (2019) 104024, <https://doi.org/10.1016/j.nanoen.2019.104024>.

[43] F. Chen, Z.Y. Ma, L.Q. Ye, T.Y. Ma, T.R. Zhang, Y.H. Zhang, H.W. Huang, Macroscopic spontaneous polarization and surface oxygen vacancies collaboratively boosting  $\text{CO}_2$  photoreduction on  $\text{BiOIO}_3$  single crystals, *Adv. Mater.* 32 (2020) 1908350, <https://doi.org/10.1002/adma.201908350>.

[44] N.N. Sun, Y. Li, X.J. Liu, X.H. Hao, High energy-storage density under low electric field in lead-free relaxor ferroelectric film based on synergistic effect of multiple polar structures, *J. Power Sources* 448 (2020) 227457, <https://doi.org/10.1016/j.jpowsour.2019.227457>.

[45] W.Y. Han, H. Zhang, D.G. Li, W.W. Qin, X.L. Zhang, S.B. Wang, X.G. Duan, Surface engineered carbon quantum dots for efficient photocatalytic hydrogen peroxide production, *Appl. Catal. B Environ.* 350 (2024) 123918, <https://doi.org/10.1016/j.apcatb.2024.123918>.

[46] S.Q. Huang, Y.G. Xu, Q.Q. Liu, T. Zhou, Y. Zhao, L.Q. Jing, H. Xu, H.M. Li, Enhancing reactive oxygen species generation and photocatalytic performance via adding oxygen reduction reaction catalysts into the photocatalysts, *Appl. Catal. B Environ.* 218 (2017) 174–185, <https://doi.org/10.1016/j.apcatb.2017.06.030>.

[47] W. Li, Y.M. Mao, Z.L. Liu, J.S. Zhang, J.H. Luo, L. Zhang, Z.A. Qiao, Chelated ion-exchange strategy toward  $\text{BiOCl}$  mesoporous single-crystalline nanosheets for boosting photocatalytic selective aromatic alcohols oxidation, *Adv. Mater.* 35 (2023) 2300396, <https://doi.org/10.1002/adma.202300396>.